Desalination and Water Treatment
www.deswater.com

doi: 10.5004/dwt.2017.11422

58 (2017) 360–367
January

Computational fluid dynamics simulation of Liqui-Cel membrane using OpenFOAM: implication for membrane distillation

Albert S. Kim[a,*], Min Soo Park[b], Ji Hee Min[b]

[a]*Civil and Environmental Engineering, University of Hawaii at Manoa, 2540 Dole Street Holmes 383, Honolulu, Hawaii 96822, USA, Tel. +1-808-956-3718; Fax: +1-808-956-5014; email: albertsk@hawaii.edu (A.S. Kim)*
[b]*Econity Co., Ltd. 640-9, Jeil-ri, Yangji-myeon, Cheoin-gu, Yongin-si, Gyeonggi-do, 449-825, Korea*

Received 23 December 2015; Accepted 9 May 2016

ABSTRACT

We investigate fluid dynamic behavior inside Liqui-Cel membrane contactors using open-sourced OpenFOAM, which provides solvers for computational fluid dynamics (CFD) software. A mesh was generated using NETGEN and converted to OpenFOAM format. In OpenFOAM, icoFoam (a solver for a transient, laminar flow of a Newtonian fluid) was used to calculate flow and pressure profiles inside the Liqui-Cel module. The inlet part of the Liqui-Cel module seems to undergo strong stress due to rapid change in feed flow direction. Feed flow tangent to pre-installed hollow fibers is rapidly developed from the inlet region to middle baffle. Rotating flow in the azimuthal direction was shortly observed from the baffle to the module outlet. Numerical simulations of Liqui-Cel CFD seem to be very challenging due to the large fiber number of hollow fibers. For fast simulation, the interior of the Liqui-Cel module can be viewed as anisotropic porous media, and transmembrane mass flux can be calculated as a perturbation of the tangential shell flow. Potential of using Liqui-Cel module for membrane distillation is discussed.

Keywords: Liqui-Cel; Membrane contactor; Gas stripping; Membrane distillation; icoFoam; OpenFOAM

1. Introduction

Desalination can be accomplished by thermal distillation and membrane separation. Thermal processes evaporate saline water at a low pressure and condense the vapor to produce distilled water. Membrane-based desalination is represented by reverse osmosis, which applies high hydraulic pressure to overcome the osmotic pressure of the saline feed water and produce fresh water [1,2]. As conventional desalination methods described above are very energy-intensive, new paradigms are proposed as combinations conventional schemes, which include membrane distillation (MD) and osmotic distillation (OD) [3–5]. In these membrane-based distillation processes, water evaporates at the feed-membrane interface, migrates through membrane pores, and condenses either at the distillate-membrane interface or in an external condenser. In this case, membrane plays a role of physical interface, where solute rejection is accompanied by the water evaporation, and water production rate is equal to the condensation rate. Efficient desalination performance universally needs a large membrane surface area per unit volume. Therefore, hollow fiber membrane modules are preferred to flat-sheet modules for higher water production rate within a small footprint.

Liqui-Cel hollow fiber membrane contactors (HFMC) have been widely used for separation of dissolved gasses (such as oxygen and carbon dioxide) from water for over 20 years [6,7]. Advantages of Liqui-Cel HFMC include (1) compact design and small size to fit into many existing units, (2) low energy consumption and capital cost, (3) reducing the need of storage tanks since chemicals are not necessary, (4) high rejection of free carbon dioxide in water, and (5) simple installation, operation, and maintenance.

* Corresponding author.

Presented at the 2015 International Environmental Engineering Conference (IEEC 2015), October 28–30, 2015, Busan, Korea.

Only a few studies, however, aimed to characterize the performance of Liqui-Cel membranes for specific gas separation or compound extraction. This must be due to geometrical and hydrodynamic complexities, stemming from the large number of hollow fibers (tens of thousands). Bocquet et al. studied effects of Liqui-Cel module configurations on extraction of aroma compounds [8]. They developed a resistance in series model to describe mass transfer of aroma compounds based on partitioning trends of the compounds between hexane and water. Agrahari et al. used Liqui-Cel HFMC for reactive extraction of succinic acid from aqueous solution [9]. In their work, a single hollow fiber is modeled to represent an average extraction performance of the Liqui-Cel HFMC, consisting of 10,200 hollow fibers. Valdes et al. concentrated noni juice using OD of Liqui-Cel HFMC [10]. Phenomenological theories were developed to describe mass and heat transfer across a hollow fiber membrane using a resistance-in-series model.

Although above studies showed reasonably good agreement between experimental observation and modeling results, the models are limited to single fiber located in an imaginary unit cell, depending on boundary conditions in the shell side of the fiber. Separations using hollow fiber membranes are difficult to characterize as momentum, and mass transfer phenomena are strongly coupled in the parallel and normal directions to the aligned fibers, and so is heat transfer in anisothermal situations. Flow patterns in the shell side is in reality not so ideal as assumed in the previous studies. In Liqui-Cel module, fluid velocity is almost perpendicular to the hollow fiber orientation near the inlet and outlet locations of the central porous pipe. Hydraulic pressure profile is not linear along the fibers and must not be symmetric about the middle baffle because large surface area of hollow fibers causes significant pressure drop. In this light, micro-scale computational fluid dynamics (CFD) is necessary to investigate local variations of fluid velocity and hydraulic pressure, and their potential impacts on separation performances of hollow fiber modules.

OpenFOAM, standing for "Open source Field Operation and Manipulation", is a C++ toolbox for continuum mechanics problems, including CFD with development of customized numerical solvers and pre-/post-processing utilities. OpenFOAM includes over 70 solvers to investigate a number of scientific and engineering phenomena of various scales, whose solvers are classified into basic CFD codes, incompressible flow, compressible flow, multi-phase flow, direct numerical simulation (DNS) and large eddy simulation (LES), combustion, particle-tracking flows, heat transfer and buoyancy-driven flows, molecular dynamics methods, direct simulation Monte Carlo methods, electromagnetics, stress analysis of solids, and finance.

Due to its numerical accuracy, good scalability, and open-source policy, OpenFOAM is very popular in modeling and simulation communities in industry and academia. Using OpenFOAM, Santos et al. [11] modeled patterns of flow fields and solute concentrations in spiral wound membrane modules; Gruber et al. studied flow and concentration polarization in forward osmosis membrane systems [12]; Al-Shagrif et al. investigated the details of hydrodynamic and heat transport conditions and their impact on temperature polarization and pressure drops for optimal design of MD modules [13]; and Wang et al. described the mass transfer across the membrane and the hydrodynamics in the flow channels of pressure-retarded osmosis [14].

Although some researchers tried to understand and improve the performance of the Liqui-Cel module, to the best of our knowledge, CFD analysis of a Liqui-Cel HFMC has not yet been conducted systematically due to its geometrical and fluid dynamic complexities, especially using OpenFOAM, a popular open-source simulation package for CFD. In this paper, we briefly report how to use OpenFOAM [15] to simulate fluid dynamics in membrane systems, scrutinize velocity and pressure profiles inside a Liqui-Cel module, and provide practical implications for MD application of Liqui-Cel HFMC.

2. Mathematical model

We aim to use the Liqui-Cel membrane for MD, especially for direct contact membrane distillation (DCMD) and vacuum membrane distillation (VMD) in the future. The MD performance depends on effective and homogeneous distribution of a feed stream to membrane surfaces, where water evaporates and starts migrating through membrane pores. In-depth understanding of fluid dynamics in Liqui-Cel module is, in this light, crucial to optimize separation performance in terms of heat and mass transfer. OpenFOAM-based CFD work of this study consists of three consecutive steps, which are mesh generation, fluid dynamics simulation, and scientific visualization with engineering implications.

2.1. Module structure

Fig. 1 shows a schematic of the Liqui-Cel membrane. Strip gas entering at one end (right-bottom) is distributed to lumen spaces of a number of hollow fibers. A fraction of the gas passes through a long hollow fiber and is collected at the other side. Water containing volatile elements such as CO_2 enters the (left-top) inlet of the central pipe. The central pipe has several holes on its surface, from which the feed stream comes out and is rapidly dispersed in the radial direction. In the middle of the containing vessel, a baffle blocks the direct unidirectional flow tangent to the packed fibers. Hollow fibers penetrate the baffle, and the strip gas flows into lumen spaces. The presence of the middle baffle elongates the hydraulic residence time and induces even distribution of

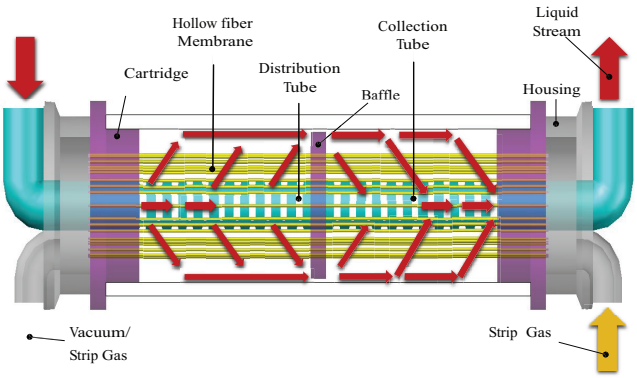

Fig. 1. Schematic of Liqui-Cel membrane.

fluid flow for its maximum contact with membrane surfaces. The radius of the baffle is very close to the inner radius of the containment vessel. The feed flow from the holes in the central pipe should pass through this very narrow cylindrical shell region between the inner wall of the container and the lateral surface of the baffle. After passing through the thin cylindrical slit region, the fluid has a slower velocity. The water stream disperses around the densely packed hollow fibers in the second half of the container and enters the central pipe though holes on the pipe surface. The baffle is the key design factor of a Liqui-Cel membrane contactor, because it determines the flow pattern, residence time, and mass transfer efficiency.

Specifications of the Liqui-Cel can be found in Table 1. In comparison to typical MD membranes and modules, a Liqui-Cel membrane has a small pore size of 0.03 μm and low porosity of 30%. Hollow fibers have the inner and outer diameters of 0.225 and 0.315 mm, respectively, and the thickness of the hollow fibers is (on the average) 0.045 mm. Total and effective length of fibers in the containing vessel are 20 and 15 cm, respectively. Diameters of the vessel wall (inner) and the middle baffle are 60.0 and 53.10 mm, respectively. Then, the gap between the baffle surface and the vessel wall is only 6.9 mm, which is about 10% of the vessel inner diameter. A rough calculation indicates that the number of fibers in the vessel is close to 15,000, and the total and effective lengths of all the packed fibers are 6.0 and 4.5 km, respectively. Surface areas based on the outer and inner diameters are 2.81 and 1.71 m^2. Operation criteria of the Liqui-Cel module suggest an input flow rate ranging from 70 to 490 ml/min. We set the flow speed of 4.42 m/s at the pipe inlet (patch 1) to have 120 ml/min of the flow rate.

Table 1
Specification of Liqui-Cel membrane. Packing fraction of hollow fibers, $\phi = 0.5$, is assumed

Membrane material	PVDF
Pore diameter (μm), d_p	0.03
Porosity (%), E	30.0
Fiber outer diameter (mm), d_o	0.315
Fiber inner diameter (mm), d_i	0.225
Fiber thickness (mm), $(d_o - d_i) / 2$	0.045
Fiber total (effective) lengths (m), l_f	0.20 (0.15)
Cartridge inner diameter (mm), D_c	60.0
Baffle diameter (mm), D_b	53.10
Cylindrical gap between baffle and cartridge (mm)	6.90
No. of fibers in cartridge (–), N_f	~14,200
Total (and effective) fiber lengths (km), $L_f = N_f l_f$	~2.842 (and 2.131)
Area (m2), $A_m = \pi dLF$, $d = d_o$ (or d_i)	2.11 (or 1.50)
Inlet pipe velocity (mm/s)	70.74
Lumen velocity (mm/s)	–3.54

2.2. Meshing technique

Fig. 2 shows the basic structure of a Liqui-Cel contactor, primarily consisting of the cylindrical container, the porous central pipe, and the middle baffle. These basic elements are drawn using AutoCAD and exported to a file of stereolithographic (STL) format, shown in Fig. 2(a). The STL file was stored in both binary and ASCII text formats, and visualized using GMSH as shown in Fig. 2(b). GMSH is a three-dimensional finite element mesh generator [16], available at http://geuz.org/gmsh/. Although both formats (ASCII and binary) are compatible to GMSH, we developed a new software program, named stl2gmsh, to directly convert the ASCII STL file to the standard GMSH format for mesh generation. (stl2gmsh can be obtained from the corresponding author.) This is because CAD-generated STL files are often mathematical incomplete due to drawing and precision errors. All the numeric information, obtained using stl2gmsh, was visualized using GMSH software, and then manually converted to a script for NETGEN [17]. NETGEN is an open-sourced, automatic 3D tetrahedral mesh generator, containing modules for geometrical optimization and hierarchical refinement. First, a mesh structure of the Liqui-Cel interior without hollow fibers was generated using NETGEN, as shown in Fig. 3(a). Spaces for the bulk fluid are shown empty. Interfaces between the bulk fluid and inner module walls are shown as the fluid volume is discretized using triangular elements since volume is discretized using tetrahedrons. As indicated in Table 1, the number of fibers in the module is of an order of O (10^4). It is very challenging to generate a mesh grid for CFD simulations with the extremely large number of hollow fibers. We generated a realistic mesh grid for fluid volume inside the Liqui-Cel module, but using only 24 fibers, as shown in Fig. 3(b). The total numbers of points is 316,591, forming 1,234,607 cells. The number of faces is 2,675,733, of which 2,263,695 faces are internal so that their difference indicates the number of interfaces between the fluid and solid volumes. The adjacent outer regions of fibers are more finely meshed with tetrahedral structures. Since the outer diameter of fibers is about 200 times smaller than the inner diameter of

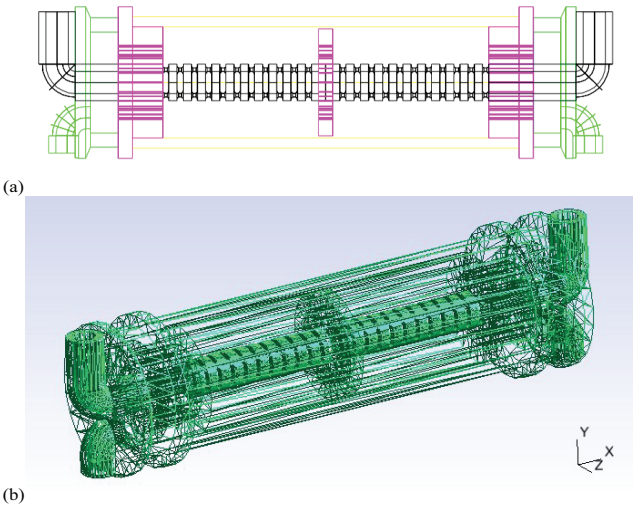

Fig. 2. Liqui-Cel structure: (a) CAD drawing snapshot and (b) plotting of stereolithographic (STL) file using GMSH.

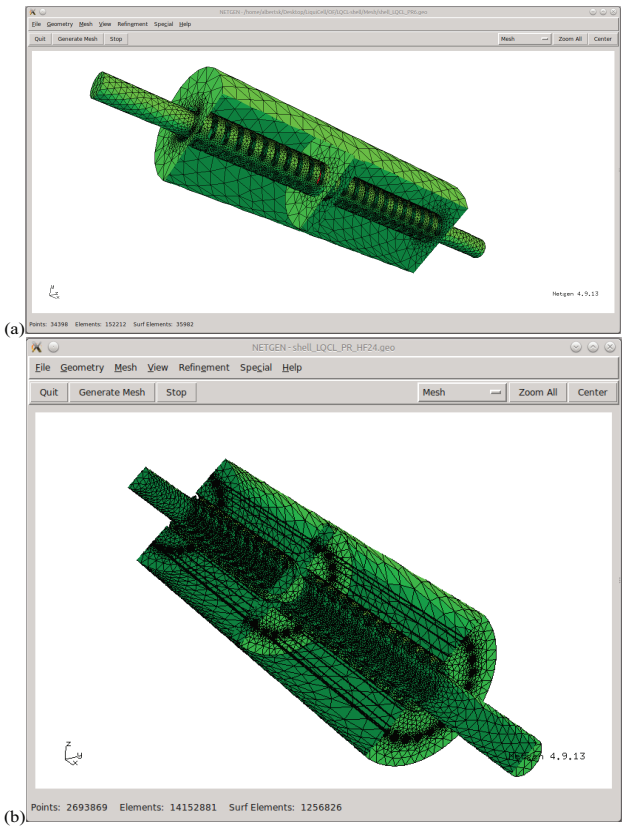

Fig. 3. Liqui-Cel meshes generated using NETGEN: (a) without hollow fibers and (b) with (only) 24 hollow fiber membranes.

the containing vessel, including more fibers in the Liqui-Cel module significantly increases computing times for meshing as well as CFD simulations (see the next section for details). Liqui-Cel meshes generated using NETGEN are converted to OpenFOAM format by standard command netgenNeutralToFoam, included in the OpenFOAM package.

2.3. CFD simulation using OpenFOAM

2.3.1. Governing equations

For flow in the central pipe, the Reynolds number is about a few hundreds, indicating that the flow is in the laminar regime. Water is typically known as incompressible fluid so that its density ϱ is assumed to be constant. In this case, density and pressure are decoupled, and the energy equation becomes independent. Then, the incompressible continuity equation is given by:

$$\nabla \cdot \vec{U} = 0 \tag{1}$$

where $\vec{U}$ is the flow field. A general form of the Navier-Stokes equation is (for momentum transfer):

$$\frac{\partial \vec{U}}{\partial t} + \nabla \cdot (\vec{U}\vec{U}) - v\nabla^2 \vec{U} = -\nabla p \tag{2}$$

where p is the pressure divided by the density, and v is the kinematic viscosity of fluid (water in this work). $\nabla \cdot (\vec{U}\vec{U})$ in the left hand side of Eq. (2) is the inertia term, which is responsible for the transfer of kinetic energy in the turbulent cascade, but less significant in the laminar regime. Since we are interested in the transient laminar flow of water, the left hand side of Eq. (2) does not vanish until the system reaches a quasi-steady state. In OpenFOAM, the non-linearity of $\nabla \cdot (\vec{U}\vec{U})$ is handled using an iterative technique, such as:

$$\nabla \cdot (\vec{U}\vec{U}) \approx \nabla \cdot (\vec{U}^0 \vec{U}^1) \tag{3}$$

where $\vec{U}^0$ is the current or initially assigned solution, and $\vec{U}^1$ is the updated solution. The iteration continues until $\vec{U}^0 = \vec{U}^1$ within a tolerable error. The absence of the pressure equation leads to a scalar constraint on the momentum equation because $\nabla \cdot \vec{U}$ is a scalar. Defining the velocity $\vec{U}$ on the cell faces (known as ϕ) gives:

$$\frac{\partial \vec{U}}{\partial t} + \nabla \cdot (\phi \vec{U}) - \nabla \cdot (v\nabla \vec{U}) = -\nabla p \tag{4}$$

where ϕ is iteratively solved to update $\vec{U}$ and p.

2.3.2. Solvers

We assumed that the feed fluid (water) is a Newtonian fluid, flowing into the Liqui-Cel module as incompressible and laminar. A transient solver for this type of fluid is icoFoam, which is employed in the present study to investigate the flow and pressure profiles inside the Liqui-Cel module. The original icoFoam does not have a scheme to dynamically change the time interval, Δt, which is typically based on Courant number. We modified the source code of icoFoam, by adding header files of "readTimeControls.H" and "setDeltaT.H", and developed a new solver, and named it icoFoam2. This new solver is equivalent to (original) icoFoam plus the time-interval adjustment scheme for faster convergence to a (pseudo) steady state. Because OpenFOAM does not have steady-state solvers, simulations should continue until the final solution is pseudo-invariant with respect to time. Using the controlDict file, users can maintain computational results of only the last a few time steps. Intermediate results from the initial state are dynamically deleted. If the fluidic system does not reach a pseudo-steady state, uses can restart the simulation at the latest time step. These advanced features of OpenFOAM allow us to accelerate CFD simulations of the Liqui-Cel module and determine optimal conditions for convergence. Directory structure and included files of this Liqui-Cel case are shown in Fig. 4, and related details can be found elsewhere.

2.3.3. Boundary conditions

Table 2 shows patches, boundary conditions, and their properties. In this work, NETGET generated six patches, that is, partial surfaces on the solid walls of the inner vessel and outer hollow fibers. Two kinds of physical boundary conditions are used for $\vec{U}$ and p at the solid and fluid surfaces. The reserved keyword of OpenFOAM boundary condition,

fixedValue, is a type of Dirichlet boundary condition to set variables constant at the boundary, for example, three constants for a flow vector $\{U_x, U_y, U_z\}$ and one constant for a scalar quantity p. For example, the no-slip boundary condition yields $\vec{U} = \{0, 0, 0\}$. Neumann boundary conditions in OpenFOAM include zeroGradient, which indicates the gradient of a quantity ψ normal to the surface is zero:

$$\nabla\Psi \cdot \vec{n} = \partial_n \Psi = 0 \tag{5}$$

where $\vec{n}$ is a unit normal vector to any surface.

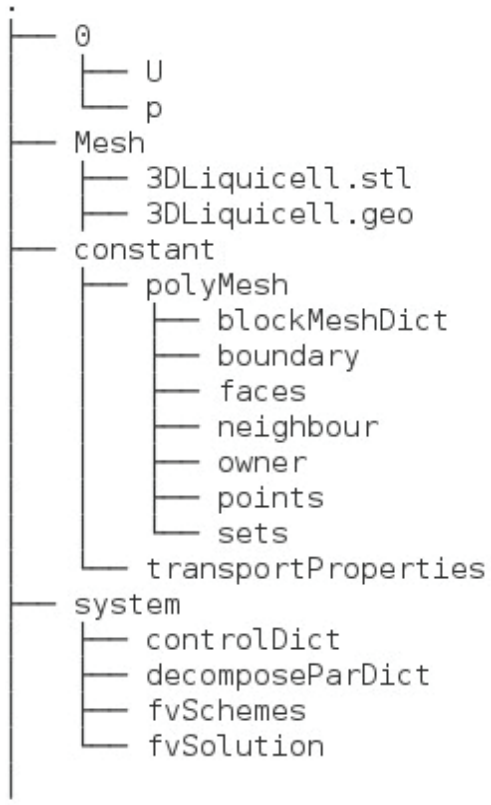

Fig. 4. Directory structure of OpenFOAM case. "0" directory contains initial and boundary conditions of flow vector U and pressure p. Mesh information is stored in "constant/polyMesh" directory, after conversion from NETGEN to OpenFOAM. Under "system", controlDict is an input file, which determines details of simulation parameters. decomposeParDict is an input file for parallel run, which is not specifically discussed in this work. Other files are typical and default files of OpenFOAM. Detailed information about the data structure can be found elsewhere (http://www.openfoam.org).

Patch 0 is a dummy to simply start the index from zero as a default initial value of NETGEN. It is included in the setup file just not to cause any running errors. No meaningful values were calculated on this patch. Therefore, setting boundary conditions of fluid velocity $\vec{U}$ and pressure p is arbitrary on patch 0. Patch 1 is the primary inlet of the vessel, where the feed flow enters with a uniform velocity. This is the left inlet surface of the central pipe, shown in Fig. 1. At this patch 1, fluid flow is assumed to be unidirectional, and the pressure is subject to the Neumann boundary condition. Patch 2 is the outlet surface of the central pipe at the right end in Fig. 1. We assume that the pipe length outside the container is long enough to stabilize the fluid flow, satisfying the Neumann boundary condition. Pressure at this patch surface is set to be $p = 0$ for simplicity. This is because only the pressure difference between the inlet and outlet boundaries of the central pipe is important instead of absolute values of p at the boundaries. Patch 3 indicates any solid surface inside the containing vessel. No-slip boundary condition is assumed to have $\vec{U} = 0$. Since the flow cannot penetrate the solid surfaces, the pressure gradient normal to the surfaces should be zero. We also simulated the water flow inside hollow fibers because our final goal is to test applicability of Liqui-Cel membrane contactor for DCMD (and VMD) operation. The inlet and outlet boundary conditions of hollow fibers are equal to those of the containing vessel. The last two columns of Table 2 indicate the numbers of faces and points belonging to each patch. Without question, the solid surfaces of the central pipe and vessel have the extraordinarily largest numbers of points forming faces.

3. Results and discussion

3.1. Pressure and velocity profiles

Fig. 5 shows a color map of pressure inside the vessel including the (left) inlet and (right) outlet parts of the porous central pipe. 24 fibers are shown as very thin threads, which are parallel to the central pipe. The periodic hole structure of the central pipe is well visualized in Fig. 5(a). Hydraulic pressure is high near the first hole at the left hand side of

Table 2
Patch properties and boundary conditions. See Table 1 for the inlet velocities at patches 1 and 4. Flow rates in the shell and lumen regions are set equal with opposite directions

	Patch	Boundary	U	p	Faces	Points
Dummy	0	Nowhere	zeroGradient	zeroGradient	0	0
Vessel	1	Inlet	fixedValue	zeroGradient	27	21
	2	Outlet	zeroGradient	fixedValue	27	21
Solid surface	3	Surface	0	zeroGradient	411,688	205,907
Hollow fiber	4	Inlet	fixedValue	zeroGradient	648	504
	5	Outlet	zeroGradient	fixedValue	648	504

the central pipe and decreases toward the middle baffle. As indicated above, the pressure and its normal gradient are zero at the outlet and inlet of the central pipe, respectively. The inlet pressure indicates the applied pressure to maintain the constant U_x at the pipe inlet. In each of the left and right-hand sides of the middle baffle, there are 42 holes. Any two paired holes are facing each other around the central line of the pipe. The baffle evenly distributes feed flow coming out of the porous central pipe, and mechanically fix the flexible hollow fiber membrane in the interior space of the vessel. When the hollow fibers are densely packed, their mechanical support might not be a serious problem, but in this case the baffle help fibers maintain certain inter-fiber distances so as not to lean on each other. Hollow fibers that touch may reduce the effective surface area, resulting in lower permeate flux. In addition, dead zones can be formed near touching fibers, significantly increasing hydraulic drag. Fig. 5(b) divides the vessel's interior into (left) inlet and (right) outlet regions along the x-direction. The 24 hollow fibers are shown in both regions. On the left inlet (top-left corner of Fig. 5(b)), streamlines coming out of the central holes become immediately normal to the central pipe and hollow fibers. After attaining a plateau profile, streamlines detour around the middle baffle by passing through the cylindrical shell region of thickness 6.9 mm between the container wall and the lateral side of the baffle. On the right side of the container (i.e., left-bottom corner of Fig. 5(b)), small vectors near the hollow fibers indicate fluid flow inside hollow fibers. Because the lumen spaces have much smaller volume with finer grids, it takes more time to develop stabilized flow fields. The flow vectors are therefore not all parallel to the hollow fibers. At the current research stage, we are satisfied with the possibility of performing CFD simulations in two different length scales, that is, within a large volume of the vessel and within many long and narrow channels of hollow fibers. We believe that the flow fields inside the hollow fibers are laminar and can be well described using the Hagen-Poiseuille equation for mass transfer simulations for the future MD research.

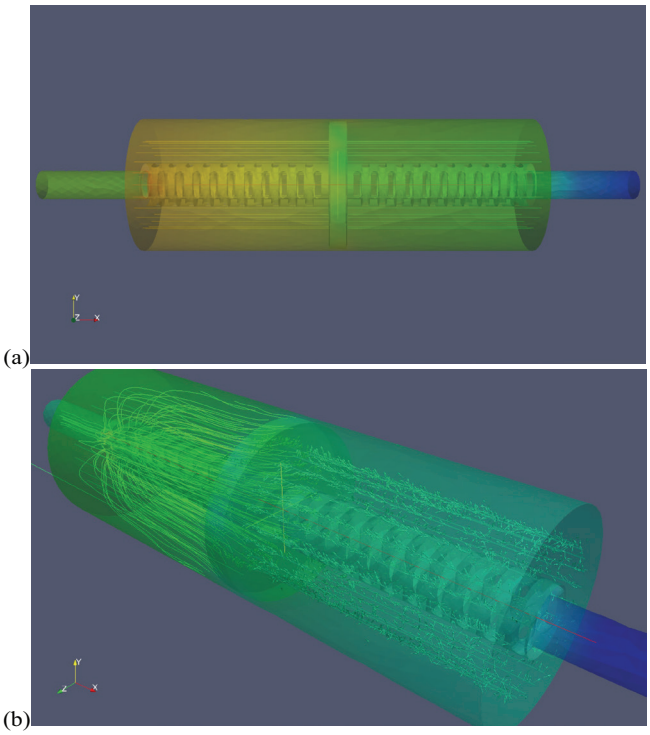

Fig. 5. (a) Pressure color map with 24 hollow fibers and (b) streamlines of pre-baffle and velocity of post-baffle spaces. The outlet pressure of the central pipe was set to zero by the boundary condition, and the mean inlet pressure of the pipe is calculated as 0.46 bar (6.67 psi). Transient fluctuation of the velocity filed is less sensitive to that of the hydraulic pressure.

3.2. Streamlines and local stresses

Due to the small number of hollow fibers, fluid flow inside the vessel does not seem to be much influenced by the hydraulic resistance caused by the installed fibers. Fig. 6(a) shows apparently different flow patterns before (left) and after (right) the baffle. Streamlines in the left section show a U shape (rotated $\pi/2$ clockwise) and those in the right side look similar to the shape of a C (or a short rotated U) in the initial stage. Both streamline groups in the left- and right-hand sides show horizontally symmetric patterns about the $x - z$ plane as well as $x - y$ plane (not shown). The velocity gradient significantly varies in magnitude with respect to location, which is highest at the gap between the baffle and the container, followed by central holes away from the baffle. Therefore, we normalize velocity vectors and show only the flow directions using blue arrows. Note that at the inlet of the central pipe (patch 1), the uni-directional flow velocity is set $\vec{U} = \{U_x, 0, 0\}$ where U_x = 70.74 mm/s. See Table 1 for details. Near the first hole of the central pipe in the inlet region, the velocity vectors are almost perpendicular to the axial direction shown in both

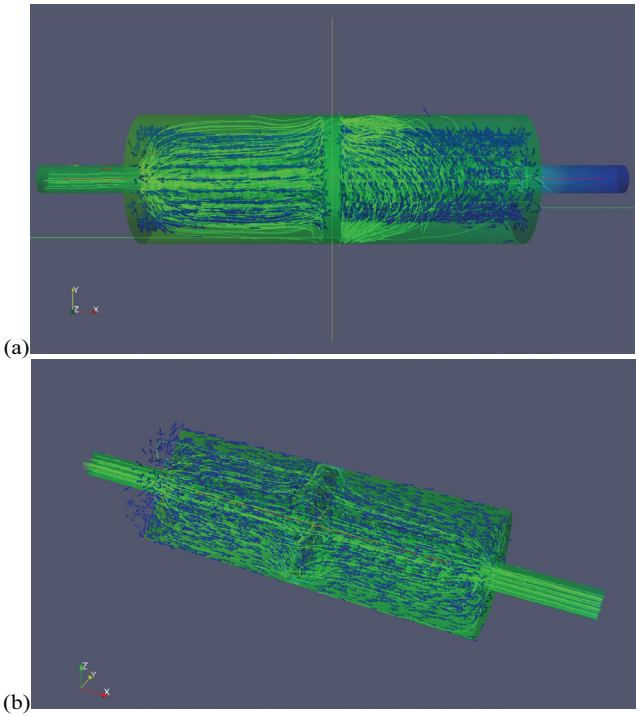

Fig. 6. Streamlines and velocity vectors in the (a) initial and (b) final stage.

Figs. 6(a) and (b). This visually indicates a transition from an axial to radial flow because central pipe is blocked by the baffle. In the middle of the left space, flow directions are mostly tangential to the axial direction until the fluid elements reach the blocking baffle. Once fluid passes over the middle baffle, it is guided toward the central pipe by the vessel wall and so promptly converges to the central holes on the right side of the vessel. Streamlines in the right outlet are much less extended in comparison to those in the left inlet space in the initial stage (Fig. 6(a)). This is because hydraulic power dissipates while the flow passes through the baffle gap region, and therefore, hydraulic pressure drops significantly. This might implies that the portions of the hollow fibers close to the right-end of the vessel are less utilized in comparison to fiber portions elsewhere. Normalized velocity vectors in the right region show a rotating behavior while those in the left region are aligned in parallel in Fig. 6(a). If the large number of hollow fibers are included and a quasi-steady state is reached, this rotating behavior of the fluid flow may not be as noticeable as shown in Fig. 6(b) for the later stage. The presence of a plethora of hollow fibers in each region additionally provides more axially guided paths for the baffle-passing fluid flow. Shortly after the simulation starts, the pressure is stabilized, and the flow field seems to have planar symmetry about the $y-z$ plane of the baffle. This symmetric behavior, in our opinion, enhances the axially oriented, well-distributed flow fields in the containing vessel even if a large number of hollow fibers are included of an order of O (10^4).

The first hole in the central pipe experiences the strongest stress due to the sudden radial thrust of the feed flow initially along the axial direction. The middle baffle is the key component that effectively disperses feed fluid between the hollow fibers and controls retention time of the feed flow. A quasi-steady state is reached first in the left side of the baffle. Flow fields, parallel to the central pipe and hollow fibers, quickly and fully developed. In the right side of the baffle, flow seems to initially rotate about the central axis and gradually develops the parallel streamlines. Streamlines look (almost) symmetrical about the plane of the baffle in the quasi-steady state. Since the module size is small and central inlet velocity is slow, the internal structure of Liqui-Cel membrane generates well-developed and stable flow fields, which must enhance the homogeneous contact of fluid with the outer walls of hollow fibers.

3.3. Implications to membrane distillation

The current work of basic CFD analysis provided key information of optimal design and operation of Liqui-Cel HFMC. Previous research reported that Liqui-Cel HFMC was successfully used for chemical extraction between liquid-liquid and liquid-gas setups across hollow fiber membranes. Due to the small sizes of inner and outer diameter of fibers and rigid installation of the middle baffle, the perpendicular flow coming out of the central holes might not strong enough to impact the mechanical stability. But, this fast velocity normal to the hollow fibers in the vicinity of feed inlet can possibly cause penetration of feed solution to the lumen spaces of hollow fibers for MD. It is inevitable to have the perpendicular flow out of the central pipe, but to minimize wetting probability in the applications of DCMD and VMD; a few hollow fibers located around the central pipe can be replaced by less impermeable ones. These will significantly reduce the wetting probability due to locally fast flow at high pressure. Several smaller baffles or flow guides can be additionally installed in the interstitial gap between the baffle side and internal wall of the containing vessel. These small baffles can change directions of fluid, when passing over the battle. This must contribute to homogeneous distribution of concentration and temperature profile around the middle baffle.

Finally, the (real) number of installed hollow fibers (of an order of O (10^4)) limits the detailed, quantitative understanding of Liqui-Cel fluid dynamics. One can picture a number of densely packed hollow fibers as anisotropic fiber-like porous media, set different hydraulic permeability in normal and tangential direction to hollow fibers, and calculate cross-section averaged tangential flow field. In general, mass flux across the membrane is at least a few orders of magnitude smaller than the tangential flow to the membrane. Since the current work showed that parallel streamlines form on each side of the middle baffle in a quasi-steady state, transmembrane mass-transfer performance of hollow fibers can be treated as a perturbative mass transfer of the un-perturbative momentum transfer in the shell region. Therefore, mass flux can be separately calculated as a post-process using the mean hydrodynamics over a single representative membrane.

4. Conclusion

We used the open-source CFD software, OpenFOAM, to investigate the fluid dynamic characteristics of a Liqui-Cel membrane contactor module. The solver icoFoam for transient, incompressible flow of a Newtonian fluid was used to simulate the flow field $\bar{U}$ and pressure p. The geometry of the Liqui-Cel module is expressed using AutoCAD, exported to STL format, and converted for GMSH visualization. Computational difficulties originate from the multi-dimensionality of Liqui-Cel module elements: hollow fiber diameters, baffle gap, and central holes. Advanced meshing tools can accelerate OpenFOAM simulations with intrinsically verified momentum and mass conservation. Use of advanced and mixed boundary conditions of OpenFOAM may enhance the stability and convergence of numerical solutions. The final mesh was generated using NETGEN with specific boundary indexes, starting with 0, because it is very challenging to use snappyHexMesh (a default mesh generator of OpenFOAM) for complex geometries such as the Liqui-Cel module.

The PVDF Liqui-Cel membrane has physical and structural disadvantages of a small pore-size, small fiber dimensions, and a low porosity. Baffle-supported packing of these hollow fibers, however, maximizes the available membrane surface area (for effective mass transfer) by providing guided steam paths with the feed flow. Flow blocking by the middle baffle significantly contributes to developing the moderately curved flow field and its homogeneous distribution. We conclude that use of the middle baffle overcomes the dimensional disadvantages of each hollow fiber by evenly distribute the feed stream and so maximizing effective membrane surface area. Future designs of membrane modules should include not only high performance membrane materials but also membrane packing that determines flow fields and regimes.

Acknowledgment

This research was supported by grant (code 13IFIP-B065893-01) from Industrial Facilities & Infrastructure research Program funded by Ministry of Land, Infrastructure and Transport of Korea government.

References

[1] H.T. El-Dessouky, H.M. Ettouney, Fundamentals of Salt Water Desalination, 2002, Elsevier Science, p. 670.
[2] I.C. Escobar, A. Schäfer, Sustainable Water for the Future: Water Recycling versus Desalination, Elsevier, Amsterdam, The Netherlands, 2010.
[3] R. Jiraratananon, R. Thanedgunbaworn, M.H. Nguyen, Vapour transport mechanism in osmotic distillation process, Int. J. Food Eng., 5 (2009) 1–19.
[4] T. Matsuura, M. Khayet, Membrane Distillation: Principles and Applications, Elsevier, New York, 2011.
[5] A. Alkhudhiri, N. Darwish, N. Hilal, Membrane distillation: a comprehensive review, Desalination, 287 (2012) 2–18.
[6] Membrana unveils its latest high-pressure Liqui-Cel contactors, Membrane Technology, 2012 (2012) 6. Available at: http://www.sciencedirect.com/science/article/pii/S0958211812700356.
[7] S. Shen, S.E. Kentish, G.W. Stevens, Effects of operational conditions on the removal of phenols from wastewater by a hollow-fiber membrane contactor, Sep. Purif. Technol., 95 (2012) 80–88.
[8] S. Bocquet, F. Gascons Viladomat, C. Muvdi Nova, J. Sanchez, V. Athes, I. Souchon, Membrane-based solvent extraction of aroma compounds: choice of configurations of hollow fiber modules based on experiments and simulation, J. Membr. Sci., 281 (2006) 358–368.
[9] G.K. Agrahari, N. Pandey, N. Verma, P.K. Bhattacharya, Membrane contactor for reactive extraction of succinic acid from aqueous solution by tertiary amine, Chem. Eng. Res. Des., 92 (2014) 2705–2714.
[10] H. Valdes, J. Romero, A. Saavedra, A. Plaza, V. Bubnovich, Concentration of noni juice by means of osmotic distillation, J. Membr. Sci., 330 (2009) 205–213.
[11] J.L.C. Santos, V. Geraldes, S. Velizarov, J.G. Crespo, Modelling of flow and concentration patterns in spiral wound membrane modules with ladder-type spacers, Desalination, 200 (2006) 395–396.
[12] M.F. Gruber, C.J. Johnson, C.Y. Tang, M.H. Jensen, L. Yde, C. Hélix-Nielsen, Computational fluid dynamics simulations of flow and concentration polarization in forward osmosis membrane systems, J. Membr. Sci., 379 (2011) 488–495.
[13] S. Al-Sharif, M. Albeirutty, A. Cipollina, G. Micale, Modelling flow and heat transfer in spacer-filled membrane distillation channels using open-source CFD code, Desalination, 311 (2013) 103–112.
[14] Y. Wang, W. He, H. Zhu, Computational fluid dynamics (CFD) based modelling of osmotic energy generation using pressure retarded osmosis (PRO), Desalination, 389 (2016) 98–107.
[15] H. Jasak, A. Jemcov, Z. Tukovic, OpenFOAM: A C++ Library for Complex Physics Simulations, International Workshop on Coupled Methods in Numerical Dynamics, IUC, Dubrovnik, Croatia, 2007, pp. 19–21.
[16] C. Geuzaine, J.F. Remacle, Gmsh: a 3-D finite element mesh generator with built-in pre- and post-processing facilities, Int. J. Numer. Methods Eng., 79 (2009) 1309–1331.
[17] J. Schöberl, NETGEN An advancing front 2D/3D-mesh generator based on abstract rules, Comput. Vis. Sci., 1 (1997) 41–52.